



Flow Dynamics of a Plane Jet Impinging on a Slotted Plate: Large Eddy Simulation

N. Kharoua[†], L. Khezzar and M. Alshehhi

Mechanical Engineering Department, The Petroleum Institute, Abu Dhabi, United Arab Emirates

[†]Corresponding Author Email: nkharoua@pi.ac.ae

(Received December 19, 2016; accepted March 15, 2017)

ABSTRACT

A turbulent plane jet impinging on a slotted surface is simulated using Large Eddy Simulation LES. The Reynolds number, based on the jet-exit velocity and width, is equal to 5435. The slotted surface is placed at a distance equal to four times the jet-exit width. Three computational grids were used to assess the accuracy of the LES simulations conducted. The interaction effects of the jet with the slot propagate away from the slot region and manifest into pressure perturbations. Interesting phenomena were observed when linking the dynamic flow features upstream and downstream of the slotted surface. LES predicted three dominant frequencies at different points from time signals of velocities and pressure. The dominant frequency of the pressure field, away from the slot, corresponds to that of coherent vortices which follow a trajectory that is far from being deviated towards the wall jet or into the slot of the impingement wall completely. Among these turbulent structures of interest, pairs of opposite, but in phase, vortices are responsible for promoting the occurrence of the throttling phenomenon. The characteristic frequencies of the pressure field are similar upstream and downstream of the impingement wall. The peaks of the fluctuating pressures, away from the slot, correlate well with the minimum flow rate through the slot which correspond to the throttling phenomenon.

Keywords: Impinging jet; Slot tone; Vortices; Fluctuating pressure; Large eddy simulation.

NOMENCLATURE

C_v	specific heat	η	kolmogorov microscale
C_w	WALE Sub-Grid Scale model constant	κ	von Karman constant
d	distance closest to the wall	λ	taylor microscale
g	gravitational acceleration	μ	fluid dynamic viscosity
H	slot width	μ_t	turbulent dynamic viscosity
L_s	mixing length for subgrid scales	ν_t	turbulent kinematic viscosity
q_j	subgrid-scale temperature flux	ρ	density
p	pressure	σ_t	ubgrid-scale turbulent Prandtl number
S_{ij}	filtered strain rate	τ_{ij}	subgrid scale stress tensor
t	time	ω	specific dissipation rate of turbulent kinetic energy
\bar{T}	filtered temperature		
\bar{u}_i	filtered xi-velocity component		
V	volume of the computational cell		
w_0	instantaneous streamwise inlet velocity		
x_i	cartesian coordinate		
y^+	normalized wall distance		
Γ	thermal conductivity		

Abbreviations

CPU	Central Processing Unit
DNS	Direct Numerical Simulation
FFT	Fast Fourier Transform
SST	Shear Stress Transport
LES	Large Eddy Simulation
RANS	Reynolds Averaged Navier Stokes

1. INTRODUCTION

The interaction of turbulent jets with different kinds of obstacles attracts more attention recently due to their broad range of industrial applications (e.g.,

Shuja *et al.*, 2007; Ziada, 2002). Turbulent jets impinging on surfaces, with one or multiple openings, are relevant to several applications including air conditioning, ventilation, solid-fuel rocket motors and whistling kettles (Matsuura and

Nakano, 2011; Assoum, 2013). The resulting flow dynamics depends on the Reynolds number and the jet exit-to-impingement surface distance in addition to the shape of the jet exit and impingement openings. This type of jet configurations can generate noise that may develop into self-sustained tones when the turbulence and sound characteristic frequencies are in phase corresponding to an establishment of a feedback loop (Ho and Nosseir, 1981). The understanding and control of the flow characteristics is essential for the control of airborne sound to reduce noise pollution in the related applications.

A series of experimental studies were conducted within the research group of University of La Rochelle on the slot tones generated by a plane jet impinging on a slotted plate. Billon *et al.* (2005) investigated the effect of the slot shape on the tones and found that when the slot bevel faces the jet flow and for a slot without bevel, the direct feedback loop does not establish. Only indirect feedback loops, resulting from the excitation of the longitudinal resonances from the flow supply duct, could be observed. As a continuation, Assoum (2013) presented more details about the dynamic field, within the space separating the jet exit and the obstacle, and its correlation with the acoustic signals. The results were summarized in spatio-temporal cross-correlation maps where a pre-whitening technique was applied to remove the most important peaks resulting from the passage of coherent structures in a frequency signal. This allowed the detection of other important phenomena, with smaller peaks, such as the feedback instabilities.

The previously mentioned contributions were based mainly on experiments. Recently, the rapid advance of computational tools motivated the research community to tackle such complex flows using Computational Fluid Dynamics CFD.

Reviews such as those of Tam (2004) or Bodony and Lele (2008) addressed the classical case of free jet to establish the best practice guidelines for the aeroacoustics simulation. It was found that the sound wavelengths and frequencies require a considerable computational cost in terms of mesh resolution, numerical tools and integration time step. Examples of such expensive simulations do exist in the literature on edge tones (Yokoyama, 2014), hole tones (Matsuura and Nakano, 2012 and 2014) and slit tones (Tam *et al.*, 2005 and 2008).

Numerical simulations of the slot tones seem to be inexistent in the literature. Since the hole tone is similar to the slot tone, insightful findings from the related literature will be described herein. Matsuura *et al.* (2011) simulated the hole tone using a direct method. They observed a previously unknown feedback loop which occurs inside the jet itself. Matsuura *et al.* (2012) elucidated the throttling mechanism for the same configuration. The throttling mechanism occurs due to the variation of pressure at the impingement hole under the effect of the passing vortices. The previous studies allowed Matsuura *et al.* (2014) to propose the suppression of

the hole tones using an obstacle placed within the wall jet at a certain distance from the hole edge depending on the flow characteristics.

Based on the literature of free and impinging jet noise, it can be concluded that acoustics increases the complexity of jet simulation due to different spatial and temporal scales compared with those of turbulence in addition to the special care needed for the boundary conditions. LES and DNS approaches are highly recommended for accuracy purposes.

In the present work, LES is used to simulate the turbulent flow generated by a plane jet impacting on a slotted plate at a Reynolds number equal to 5435, based on the jet-exit velocity and width. The distance separating the jet exit and the slotted surface is four times the jet-exit width. This problem was studied experimentally by Assoum (2013) focusing on the free jet and impingement regions. The present LES simulation is intended to complement the experimental study from a flow dynamics viewpoint only while the acoustic field would require unavailable prohibitive computational resources. More details about the behaviour of the coherent vortices are presented to identify those with the major contribution in the pressure field disturbances away from the slot.

The numerical approach adopted is presented first followed by the discussion of the results and conclusions.

2. SIMULATION APPROACH

The simulation approach consists in solving the filtered compressible Navier-Stokes equations for the purpose of predicting the main turbulence features of the flow in addition to pressure fluctuations. The mathematical formulation is presented first followed by the details of the geometry, computational grid, numerical tools and simulation steps.

2.1 Mathematical and Numerical Modeling Assumptions

The Large Eddy Simulation approach, as implemented in ANSYS FLUENT 16.2 (ANSYS Inc., 2015), is used in this study and is based on the Wall-Adapting Local Eddy-Viscosity (WALE) model under Favre-averaging of the Navier-Stokes equations.

First, the flow variables are decomposed into large-scale components (denoted here by the overbar) and small subgrid scale components by employing a top-hat filtering operation. For any variable ϕ , the filtered form is:

$$\bar{\phi}(x) = \int_{fluid\ domain} \phi(x') \mathcal{G}(x, x') dx' \quad (1)$$

The finite volume technique used here provides the filtering required in an implicit manner. Hence for any variable say ϕ we have:

$$\bar{\phi} = \frac{1}{\gamma} \int_{\gamma} \phi(x') dx' \quad (2)$$

where γ is the volume of the computational cell. The filter function implied by the above operation is a top-hat filter:

$$G(x, x') = \begin{cases} \frac{1}{\gamma} & \text{if } x' \in \gamma \\ 0 & \text{otherwise} \end{cases} \quad (3)$$

In ANSYS FLUENT density-weighted or Favre averaged equations are solved. The Favre operator for any variable ϕ is defined thus:

$$\tilde{\phi} = \frac{\bar{\rho\phi}}{\bar{\rho}} \quad (4)$$

where ρ is the density

The following filtered Navier-Stokes equations for variable density flows are obtained:

$$\frac{\partial \bar{\rho}}{\partial t} + \frac{\partial}{\partial x_i} (\bar{\rho} \tilde{u}_i) = 0 \quad (5)$$

$$\frac{\partial}{\partial t} (\bar{\rho} \tilde{u}_i) + \frac{\partial}{\partial x_j} (\bar{\rho} \tilde{u}_i \tilde{u}_j) = -\frac{\partial \bar{p}}{\partial x_i}$$

$$\frac{\partial}{\partial x_j} \left[\bar{\mu} \left(\frac{\partial \tilde{u}_i}{\partial x_j} + \frac{\partial \tilde{u}_j}{\partial x_i} \right) - \frac{2}{3} \bar{\mu} \frac{\partial \tilde{u}_l}{\partial x_l} \delta_{ij} \right] \quad (6)$$

$$- \frac{\partial \tau_{ij}}{\partial x_j}$$

where μ is the dynamic viscosity, p is the pressure, τ_{ij} is the subgrid stress tensor. The fluid properties are obtained from the ideal gas law for the density, the kinetic theory for the thermal conductivity and the Sutherland's law for the laminar viscosity (ANSYS Inc., 2015).

The subgrid stress, obtained according to the Leonard's decomposition and accounting for the unresolved scale contribution, is defined by:

$$\tau_{ij} = \bar{\rho} \tilde{u}_i \tilde{u}_j - \bar{\rho} \tilde{u}_i \tilde{u}_j \quad (7)$$

This term is then split into an isotropic and deviatoric parts:

$$\tau_{ij} = \left(\tau_{ij} - \frac{1}{3} \tau_{kk} \delta_{ij} \right) + \frac{1}{3} \tau_{kk} \delta_{ij} \quad (8a)$$

The deviatoric part is modeled based on the Boussinesq hypothesis while the isotropic part is added to the filtered static pressure term.

$$\tau_{ij} = \left(-2\mu_t \bar{S}_{ij} - \frac{1}{3} \bar{S}_{kk} \delta_{ij} \right) + \frac{1}{3} \tau_{kk} \delta_{ij} \quad (8b)$$

The eddy viscosity is modeled according to the WALE model which is intended to mimic the appropriate wall asymptotic (y^3) and has the advantage of returning a zero turbulent viscosity for laminar-flow regions in shear flows (ANSYS Inc.,

2015).

$$\mu_t = \bar{\rho} L_s^2 \frac{\left(S_{ij}^d S_{ij}^d \right)^{3/2}}{\left(\tilde{S}_{ij} \tilde{S}_{ij} \right)^{5/2} + \left(S_{ij}^d S_{ij}^d \right)^{5/4}} \quad (9)$$

where μ_t is the subgrid-scale turbulent viscosity and S_{ij} is the strain rate tensor based on the resolved velocity field. L_s is the mixing length for subgrid scales defined as

$$L_s = \min \left(kd, C_W V^{1/3} \right) \quad (10)$$

The tensor S_{ij}^d is defined as

$$S_{ij}^d = \frac{1}{2} \left(\tilde{g}_{ij}^2 + \tilde{g}_{ji}^2 \right) - \frac{1}{3} \delta_{ij} \tilde{g}_{kk}^2 \quad (11)$$

$$\tilde{g}_{ij} = \frac{\partial \tilde{u}_i}{\partial x_j} \quad \text{where}$$

The filtered energy equation is written as:

$$C_v \frac{\partial \bar{\rho} \tilde{T}}{\partial t} + C_v \frac{\partial \bar{\rho} \tilde{u}_j \tilde{T}}{\partial x_j} = -p \frac{\partial \tilde{u}_j}{\partial x_j} + \frac{\partial}{\partial x_j} \left(\bar{\Gamma} \frac{\partial \tilde{T}}{\partial x_j} \right) - C_v \frac{\partial q_j}{\partial x_j} \quad (12)$$

where C_v is the specific heat and Γ is the thermal conductivity

The subgrid-scale heat flux is defined as

$$q_j = \overline{\rho u_j T} - \bar{\rho} \tilde{u}_j \tilde{T} \quad (13)$$

and is calculated using the subgrid-scale turbulent Prandtl number

$$q_j = \frac{\nu_t}{\sigma_t} \frac{\partial \tilde{T}}{\partial x_j} \quad (14)$$

2.2 Geometry and Mesh

The Cross-section of the geometry is presented in Fig. 1. The configuration corresponds to one of the cases studied experimentally by Assoum (2013). The slotted plate is placed at a distance equal to four times the jet-exit width (inlet of the computational domain). The slot width $H=10\text{mm}$.

Above the impingement plate, the computational domain has been extended laterally to 14 times the jet-exit where the wall jet develops. Downstream of the impinging plate, the domain has been extended twenty times the jet-exit width in the streamwise direction and 8-14 times laterally. These dimensions were chosen based on URANS 3D simulations to identify the appropriate locations of the pressure boundary conditions with negligible effects of the jet flow. The slot is beveled as described in Fig. 1 identically to the experimental configuration.

A multi-block structured hexahedral grid was generated in most of the computational domain (Fig. 2).

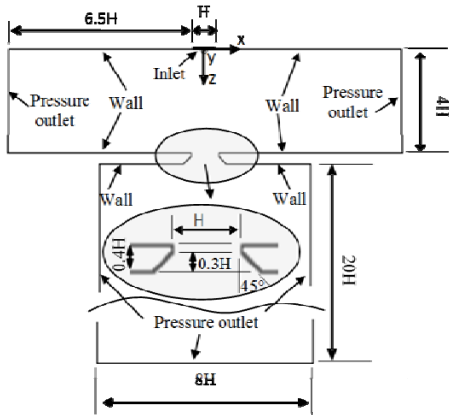


Fig. 1. Geometry and boundary conditions (dimensions in mm).

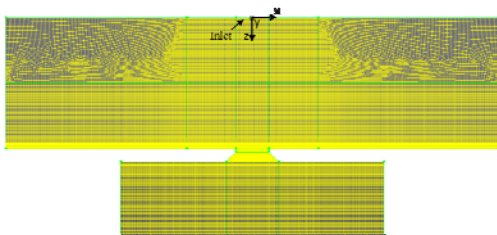


Fig. 2. Computational grid.

Three computational grids were generated and assessed from a LES viewpoint which is not intended to represent a classical grid independency test such as for RANS based simulations. In fact, the objective in LES is to generate an optimal mesh size within the Taylor microscale range allowing the capture of the most energetic turbulent structures (Ghosal, 1999; Celik *et al.*, 2005). Otherwise, a classical grid independency would yield a DNS simulation altering the optimization approach of LES. Sagaut (2006) listed some parameters usually used to assess the efficiency of a computational grid for LES simulations such as the turbulence length and time scales, the percentage of resolved turbulent kinetic energy, a priori validation and/or posteriori validation. In the present study, the mesh is assessed through the Kolmogorov (Equation 15) and Taylor (Equation 16) microscales (Pope, 2000) in addition to the posteriori validation based on the available experimental data.

The computational domain was divided into 3.9, 19 and 21.7 million cells representing coarse medium and fine meshes, respectively. The grid was refined in the two free jet regions upstream and downstream of the impingement plate, the impingement region, and the two wall jets. Approaching the pressure boundaries (Fig. 1) the mesh was stretched with a maximum aspect ratio of 5. Based on a RANS simulation (K- ω SST model), the ratio of the mesh size to the Kolmogorov scale was less than 14, 10 and 8 for the coarse, medium and fine grids, respectively. The literature (e.g., Hadžiabdić and Hanjalić, 2008) recommends a ratio smaller than 12 which is satisfied by the medium and fine computational meshes generated. In addition, the computational cells are smaller than

twice the Taylor microscale in the whole domain apart from the wall-adjacent nodes for the coarse and medium grids while less than half the Taylor microscale for the fine grid.

The non-dimensional distance from the curved wall (y^+) was smaller than 1 in the wall jet region for all the grids.

$$\eta = \left(\frac{v^3}{\varepsilon} \right)^{1/4} \quad (15)$$

$$\lambda \approx \left(10\nu \frac{k}{\varepsilon} \right)^{1/2} \quad (16)$$

2.3 Boundary Conditions

At the inlet of the computational domain, a velocity profile was imposed as shown in Fig. 3. A turbulence intensity, equal to 2%, was prescribed based on the experimental work of Assoum (2013). The spectral synthesizer technique (ANSYS Inc., 2015) was used for the generation of fluctuating velocity components.

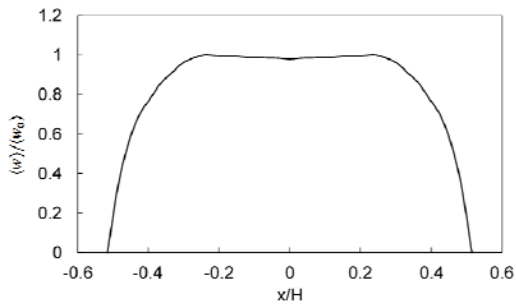


Fig. 3. Normalized mean velocity profile imposed at the inlet.

Non slip boundary condition was imposed at the walls.

An atmospheric pressure was imposed at the remaining lateral boundaries of the computational domain in conjunction with the Non-Reflecting Boundary Condition option (ANSYS Inc., 2015) to avoid the reflection of spurious pressure waves. A periodic boundary condition is applied at the opposite surfaces in the y direction to reduce the computational domain and optimize the computational grid. The distance separating the parallel surfaces is equal to 5 times the jet exit, for the coarse and medium grids, and 2.5 times the jet exit for the fine mesh. The reduction of the computational domain size in the periodic direction allowed to refine the medium mesh without increasing the total number of cells noticeably. Versteeg and Malalasekra (2007) mentioned that this distance should be at least twice the turbulent length scale of the problem to ensure a minimal effect of cutting the real configuration using periodic boundary conditions. Assoum (2013) found that, similarly to the present simulation, the size of the largest turbulent structures is smaller than the jet exit width which satisfies the previously mentioned condition.

2.4 Numerical Tools

In the present work, the bounded central difference scheme (ANSYS Inc., 2015) was used for both space and time discretization. In addition to the previously-mentioned limitations of the available computational resources, in terms of mesh refinement, the implemented discretization schemes are limited to a second order accuracy that is sufficient for the simulation of the dynamic field while higher order schemes are still necessary for the prediction of the acoustic field. This is another reason that prevented this study to be extended to the prediction of the acoustic field as well.

2.5 Simulation Strategy

The simulations were conducted in four steps. A steady flow field was, first, obtained using the $k-\omega$ SST model to generate a good first guess for the transient LES simulations. Then, transient LES simulations were run with time step equal to 10^{-5} s until a statistical convergence was reached after 10 cycles based on a characteristic frequency of 100Hz extracted from the present case frequencies. After that, another transient simulation was conducted while imposing the Non-Reflecting Boundary Condition with a smaller time step (2.5×10^{-6} s) during 5 cycles. The last step consisted in collecting the flow statistics during more than 10 cycles. The statistical convergence was assessed through time-averaged and rms variables monitored on few points shown in Fig. 4.

The simulations were run using 48, 96 and 144 parallel processors for the coarse, medium and fine grids, respectively, during approximately 3000 hours of CPU time. The pcmpi library was used as message passing interface.

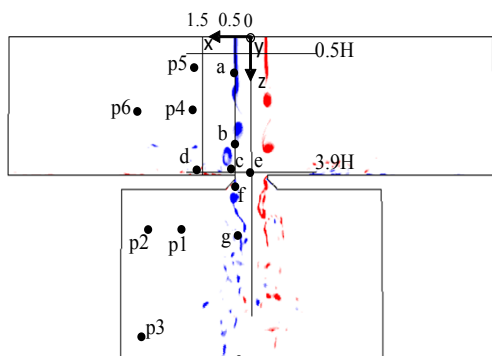


Fig. 4. Points and lines used for results presentation.

Table 1 non-dimensional positions of the probe points

Point	a	b	c	d	e	f	g
x/H	0.5	0.5	0.6	1.7	0.0	0.5	0.4
z/H	1.1	3.2	3.9	3.9	4.0	4.4	5.8

Point	p1	p2	p3	p4	p5	p6
x/H	2.1	3.2	3.4	1.8	1.8	3.5
z/H	5.6	5.6	8.7	2.2	1.0	2.2

Table 1 shows the exact positions values of the points. The reference is (0,0) in Fig. 4.

Figure 5 illustrates a sample of the development of the time-averaged and rms variables with time covering the abovementioned simulation phases. The locations of the points considered can be found in Fig. 4.

3. RESULTS AND DISCUSSION

The results section is divided into two main parts. The first part is devoted to the time-averaged field where profiles of the mean and r.m.s of the streamwise velocity component are presented for validation purposes.

In the second part, the instantaneous field is presented to show the main transient features of the flow field and the characteristic frequencies of the fluctuating pressure field collected from different points in the computational domain in addition to the correlation between the two fields. It is worth noting that the experimental measurements were limited to the region upstream of the slotted plate.

In the present work, results from the LES simulations are extended to include the region downstream of the slot as well. Six points (named p1-p6), shown in Fig. 4, were used to collect the fluctuating pressure signals away from the slot region and instantaneous velocity signals were collected at different points in the computational domain to explore the evolution of the characteristic frequencies at different regions of the computational domain. In addition, lines at specific regions were used to present the mean velocities for validation purposes or instantaneous velocity and pressure for time-space plots. The points and lines in Fig. 4 will be referred to throughout the results section. The jet width is taken as a reference length scale.

3.1 Time-Averaged Field

Figure 6 illustrates profiles of the streamwise (z direction) component of the mean and fluctuating velocities at two different z-positions from the jet exit (0.5H and 3.9H) which correspond to locations close to the jet exit and slotted plate, respectively.

The overall comparison of the previously mentioned variables with the experimental measurements of Assoum (2013) is acceptable. The fluctuating velocity profiles (Fig. 6c and d) exhibit some discrepancies. The LES simulations under-predict the fluctuating velocities close to the jet exit at 0.5H (Fig. 6c) by up to 57% and over-predict them close to the slotted plate at 3.9H (Fig. 6d) by up to 37%.

Based on the similar profiles obtained using different grids, only the results obtained using the coarse grid will be presented in the following section unless otherwise stated.

3.2 Instantaneous Field

Assoum (2013) investigated the relation between the vortices behavior upstream of the slot and the

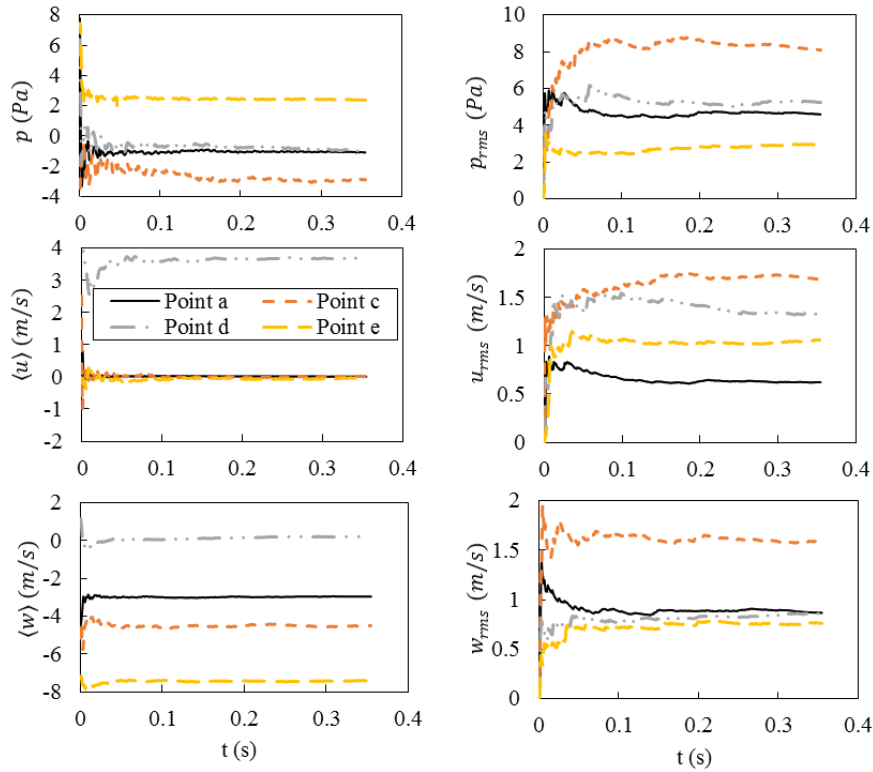


Fig. 5. Convergence of the statistical variables.

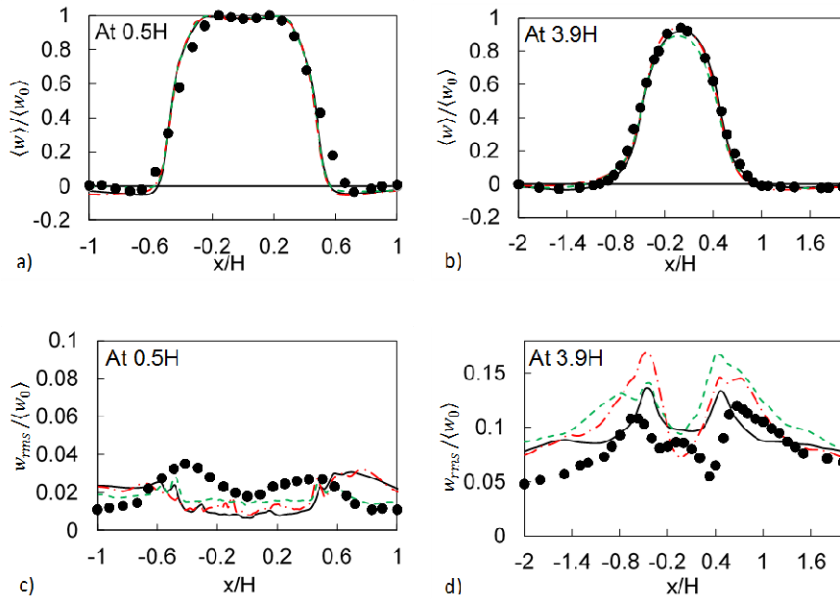


Fig. 6. a and b: Mean velocity profiles, c and d: fluctuating velocity profiles (see Fig. 4 for positions).

characteristic frequencies and sound levels of the acoustic field at one point downstream of the slotted plate. Although the present simulation is not intended to resolve the acoustic field, it explores the behavior of the vortices and their interaction with the slot which affects the pressure field away from the slot based on temporal signals of different variables at different locations of the computational domain (see Fig. 4). In the present LES simulations,

a Reynolds number equal to 5435 and a distance equal to $4H$ were chosen based on the fact that this combination was found, in the experiments of Assoum (2013), to yield a noisy configuration with several flow field phenomena associated with the slot tones.

In this flow, vortices are generated inside the plane shear layers surrounding the free jet region due to

Kelvin-Helmholtz instabilities. They grow, sometimes in pair and in phase and interact with the slot. Fig. 7 illustrates the positions of vortices having their axis in the y direction obtained from the superposition of instantaneous y vorticity contours.

Assoum (2013) observed two main vortex trajectories which are shown in Fig. 7 by the white lines curves. These represent vortices that either deviate towards the wall jet region or penetrate through the slot. However, the experimental measurements and subsequent observations were limited to the space between the jet exit and the impingement wall. The LES simulation allowed tracking the vortices positions in a larger domain which encompassed the space below the solid plate.

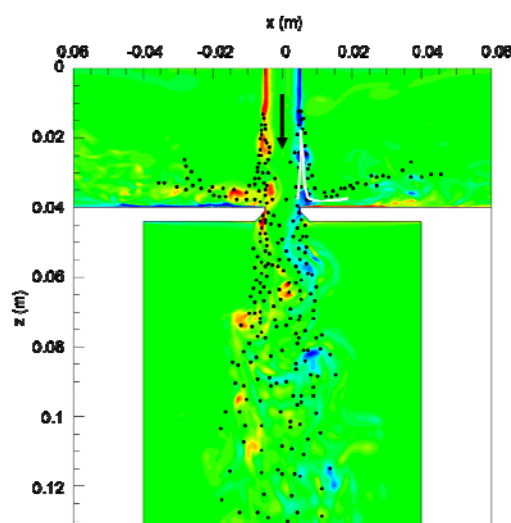


Fig. 7. Positions of vortices (black dots) superimposed on y vorticity contours (white curves from experiments of Assoum, 2013).

Although uncertainties are expected in the prediction of the exact positions of vortices, the main trajectories, observed experimentally, are well predicted by LES as well.

The simulation shows that the laterally deviated vortices in the wall jet region, tend to be displaced away from the impingement wall as they move downstream. The experimental results do not include this region unfortunately. In the central region of the jet, upstream of the slot, vortices might access the jet core occasionally. Downstream of the slot (i.e., below the plate), the vortices generated inside the initial shear layer (close to the jet exit) and those generated at the slot lips form a plume of vortices which grows laterally by entrainment with streamwise distance.

Frequency spectra of fluctuating pressure p' are presented in Fig. 8 for six points (points p1-p6 illustrated on Fig. 4) to assess the characteristic frequencies of the pressure field at several locations away from the slot region.

A dominant peak of approximately 200Hz in all the points used as probes is seen apart from point p1

where the dominant frequency is about 100Hz is predicted.

The characteristic frequencies of the turbulent structures are explored, now, to investigate their correlation with the fluctuating pressure signals of Fig. 8. Fig. 9, illustrates the frequency spectra obtained from the simulations at different points of the computational domain (see Fig. 4 for the positions of the points).

Each row of figures represents the frequency spectra at a certain point extracted from the time signals of u , w and p' , respectively.

At point a, corresponding roughly to the point of generation of vortices in the free jet region, the dominant frequency is about 300Hz. Two other characteristic frequencies can be seen and are equal to 100Hz and 200Hz, respectively. At point b, the three characteristic frequencies persist. At point c (very close to the impingement wall), the three characteristic frequencies are still present, however, the damping of w velocity (perpendicular to the wall) alters the frequency spectrum noticeably.

At point d (wall jet), the u velocity signal yields two characteristic frequencies (100Hz and 200Hz) while the w velocity signal yields two characteristic frequencies equal to 200Hz and 300Hz, respectively, and the p' signal still exhibits the three frequency peaks.

At point e (slot), the three initial characteristic frequencies reappear while only one distinguished peak, at 200Hz, is seen for the u velocity and p' signals. At point f (in the shear layer downstream of the slot lip), the initial three frequency peaks persist for the u velocity and p' signals while a unique peak, for a frequency equal to 100Hz, appears for the w velocity signal. The status is quite similar for point g (farther downstream of the slot) with the disappearance of the peak at 300Hz from the p' signal. Overall, the same three dominant peaks were seen in the p' signals at points p1-p6 (Fig. 8).

Animations showed that the frequency of vortex generation is equal to about 300Hz. The deviation of the vortices either towards the wall jet or the slot yields different vortex positions if we consider one point as a reference. For example, point b (Fig. 4) detects the passage of the vortices either at its left or right side. The animations showed, also, that the vortices can follow a straight downward trajectory for which the vortex center coincide with the coordinates of point b. This oscillating-like motion makes the passage of the vortices at exactly point b more frequent than the passage of vortices at its left or right sides. As a conclusion, the vortices are generated at a frequency equal to about 300Hz. The passage of the vortices at the left or right side of a reference point within the shear layer central plane yields a frequency equal to about 100Hz while their more frequent passage at the point coordinates (shear layer central plane) yields a frequency equal to about 200Hz. The frequency of 200Hz is, approximately, dominant at points p1-p6 as shown in Fig. 8. This suggests that the pressure fluctuation

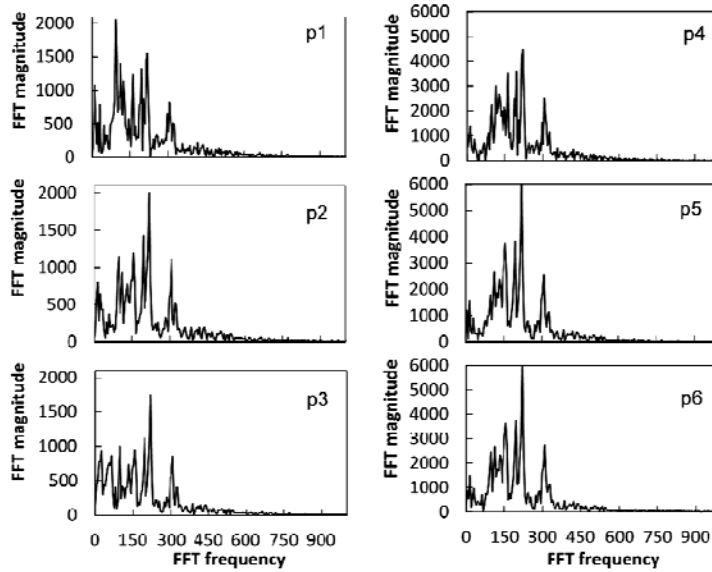


Fig. 8. Frequency spectra from p' time signals at different points of the domain (see Fig. 4 for positions of points).

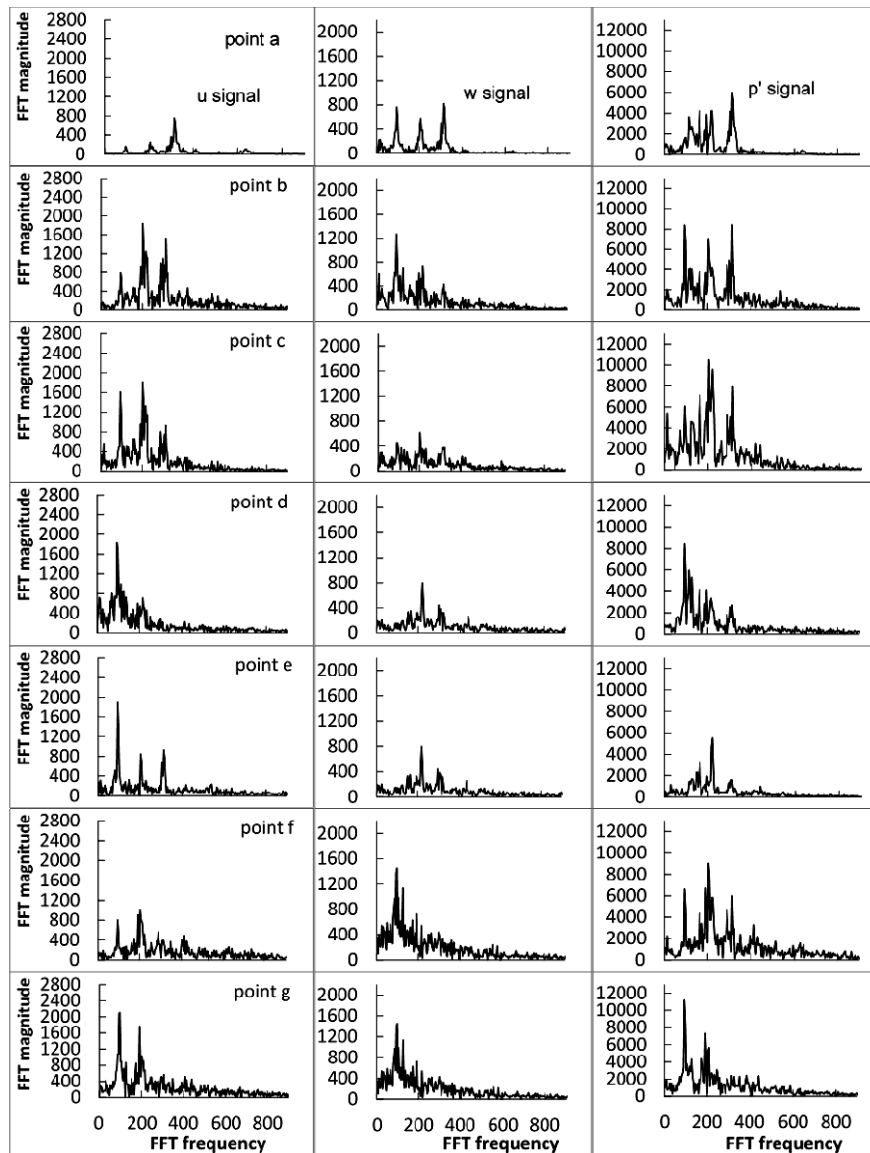


Fig. 9. Frequency spectra at different points: rows) points a-g, columns) variables w , u and p' .

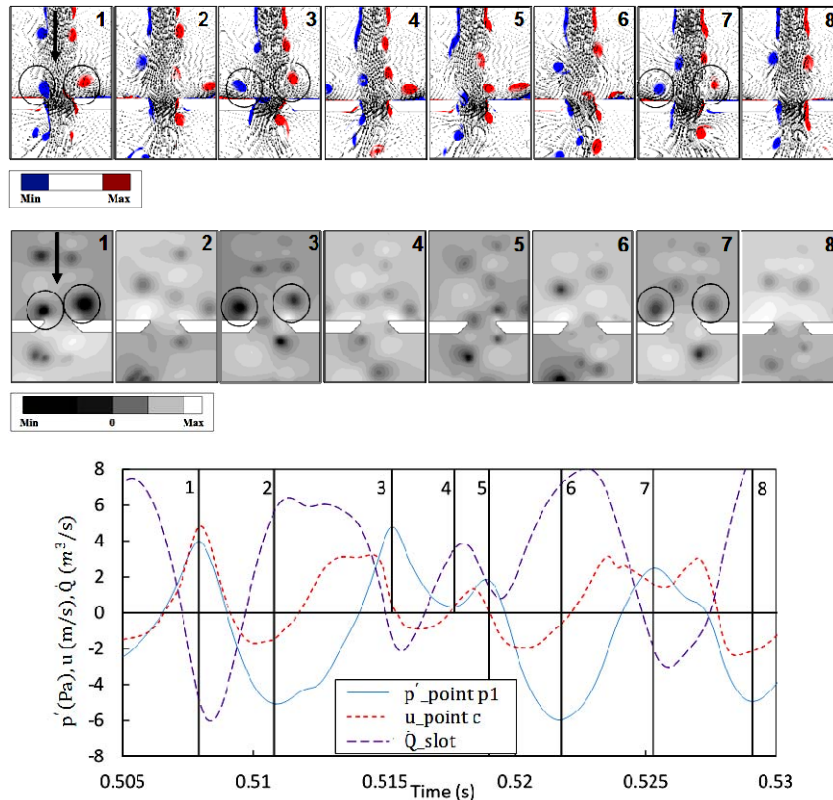


Fig. 10. Top) y vorticity contours superimposed on velocity vectors. Middle) p' contours, Bottom) time signals of p' , u and flow rate at different points (see Fig. 4 for positions of points).

peaks, away from the slot, are strongly related to the behavior of the vortices which do not deviate, completely, with the wall jet or in the slot.

To further explore the correlation between the vortices behavior and the pressure far field, contours of y vorticity and p' in conjunction with timeline variation of p' , u and the flow rate through the slot Q are plotted in Fig. 10.

The positive and negative peaks of p' at point p1 are identified by vertical lines. The contours are extracted at the time steps corresponding to the previously mentioned peaks of p' at point p1 (see Fig. 4). Fig. 10 is intended to show the flow field status when p' time variation exhibits peaks. It is clear that the positive peaks of p' , at p1, correspond to the presence of two opposite vortices close to the slot and the minimum flow rate (times 1, 3 and 7).

Assoum (2013) observed a similar phenomenon and explained it by the occurrence of flute sound effect when the two opposite vortices are close to the impingement slot causing a throttling phenomenon like.

Matsuura *et al.* (2012) also noticed the throttling phenomenon and explained it by the alternate impingement of low and high pressure regions near the slot lips.

This causes the high pressure regions, when penetrating the slot, to throttle the flow through it. These phenomena can be seen in Fig. 10 where the

minimum flow rates through the slot correspond to the presence of the high pressure regions within the slot while the low pressure regions (vortices) are close to the two upper sides of the slot.

Figure 11 depicts the time-space plots of p' at four x/H positions (see Fig.4 for the positions). Figure 12 complements Fig. 11 by showing the corresponding snapshots of p' and y vorticity contours. The time-space plots of p' show where high and low pressure regions are generated and how they are convected. The convection velocity corresponds to the slope of the plots at characteristic positions ($x/H=\pm 0.5$ in this case).

The plots illustrate, also, the characteristic frequencies through the alternate low and high pressure regions with time. From the positions $x/H=0$ (centerline) and $x/H=1.5$ (outside the jet region) an approximate frequency of 200Hz can be observed through the alternate peaks of p' . This value was, also, observed at different points of the domain as seen in Figs. 8 and 9. As noticed by Matsuura *et al.* (2011), an important observation here is that the pressure waves propagate inside the jet as well.

The plots reveal roughly three zones from the jet exit towards the impingement wall. The first zone ($z/H<1$) corresponds roughly to the first part of a free shear layer developing from the jet-exit lip without apparent coherent vortices. Then, another zone ($z/H=1-3$) includes the generation and

convection of vortices. The last zone ($z/H=3-4$) coincides with the impingement of the low and high pressure fluctuation regions on the slotted surface.

Before discussing the time-space plots, it is important to precise that low p' regions correspond to the location of the vortices while the high p' regions correspond to the space between successive vortices. The co-rotating successive vortices entrain two opposite fluid streams which impact in the separating space causing the high pressure regions. Thus, the vortex intensity and the distance between successive vortices affect the presence and magnitude of the high pressure regions.

In Fig. 11, at $x/H=0$ (jet centerline), the alternate low and high pressure regions are almost vertical columns with noticeable peaks at about $z/H=1.5-2.5$ and close to the slot at $z/H=3.5-4$. These peaks correspondent to the interaction of the low and high p' regions from both sides of the jet within the opposite shear layers (see at $x/H=\pm 0.5$).

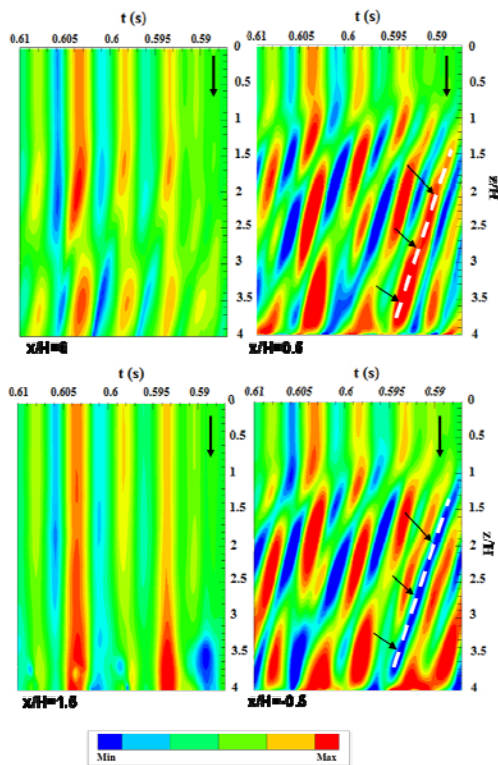


Fig. 11. Space-time plots of pressure fluctuations at different positions x/H upstream of the impingement wall.

For example, Fig. 12a illustrates the presence of two vortices close to the jet centerline which causes the low p' regions at $x/H=0$ and $z/H=3.5$ when $t=0.596s$ and $t=0.601s$, respectively, in Fig. 11.

The fact that the low and high p' regions are not perfectly vertical is due to the oscillation of the jet as shown in Figs. 12a and 12b.

At $x/H=\pm 0.5$ (shear layers), the alternate low and high p' regions are convected with a velocity equal to approximately 4.17 m/s (calculated from the slop

of the inclined low and high p' regions shown by dashed lines in Fig. 11) which represents half the jet velocity. The oscillations of the jet are also responsible for the discontinuities exhibited by the convected low and high p' regions.

In fact, two high and low pressure regions (shown by arrows in Fig. 11) travel through an almost straight trajectory as illustrated in Fig. 12b. The continuous high pressure region, in Fig. 11 at $x/H=0.5$, corresponds to the high pressure region tracked in Fig. 12b, with arrows, at different time steps. Similarly, the continuous low pressure region in Fig. 11, at $x/H=-0.5$, corresponds to the vortex tracked in Fig. 12b, with arrows, at different time steps.

At $x/H=1.5$, alternate perpendicular columns of p' correspond to pressure waves transmitted outside the jet region (fluid almost at rest). However, the presence of the wall jet in the zone $z/H=3-4$ causes the noticeable low and high p' regions such those at $t=0.589s$ and $t=0.5935s$, respectively.

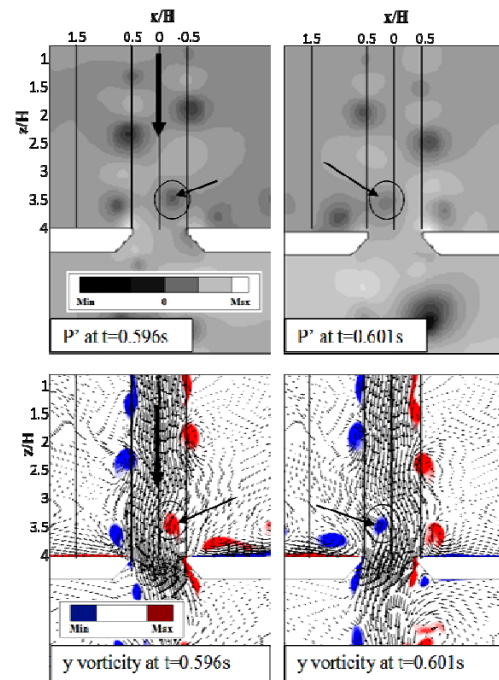


Fig. 12a. Vortices approaching the jet centerline.

4. CONCLUSIONS

Large Eddy simulation LES was used to simulate a turbulent plane jet impinging on a slotted surface. Similar results were obtained using different computational grids in terms of resolution.

The centers of the vortices coincide with low pressure regions while high pressure regions reside between each pair of successive vortices, within the same shear layer, leading to the continuous succession of low and high pressure regions from the vortex generation to their impingement on the slotted surface along the opposite shear layers on either sides of the jet.

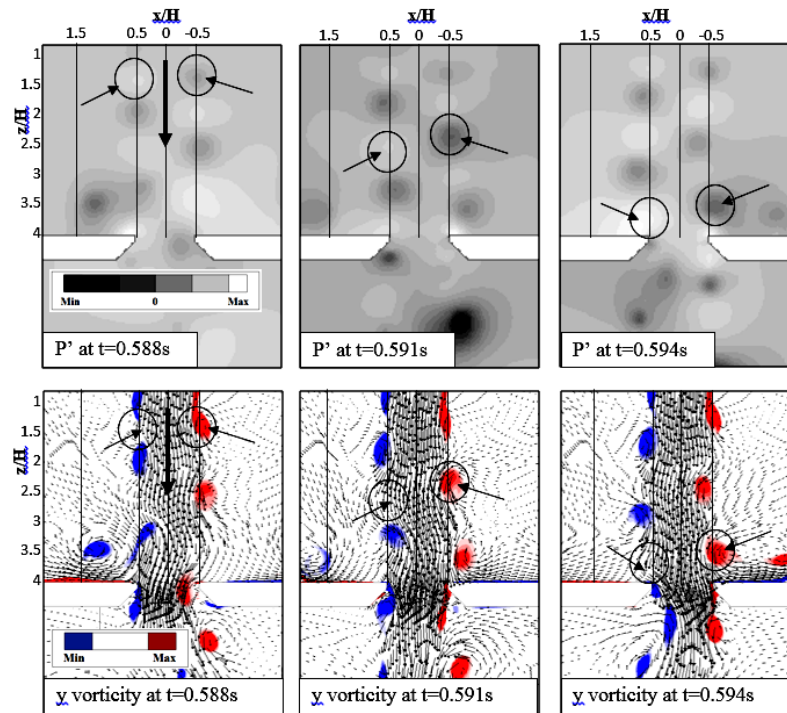


Fig. 12b. Vortices with a straight trajectory.

The peaks of the fluctuating pressures p' away from the slot correlate well with the minimum flow rate through the slot. It was found that these peaks correspond to the presence of two opposite, but in phase, vortices close to the slot. Consequently, the two high pressure regions, immediately downstream of the two preceding opposite vortices, penetrate in the slot and cause the throttling phenomenon to occur which is responsible for the noticeable peaks of fluctuating pressure that propagate in the rest of the domain.

The pressure waves propagate, backward, inside the jet as well although their effects are not as important as those outside. The simulations predicted three dominant frequencies at different points from time signals. It was found that the highest frequency, among the three characteristic frequencies, corresponds to the generation of vortices within the opposite free-shear layers close to the jet exit. Then, the oscillation of the shear layer downstream causes the vortices to follow different trajectories which are the source of the two other characteristic frequencies at different locations.

The vortices follow different paths by moving into the wall jet region, penetrating into the slot or impinging on the slotted surface. Comparing the characteristic frequencies of p' signals, at different locations outside the jet flow upstream and downstream of the impingement surface, it appeared that they are strongly related to the behavior of the vortices which tend to follow a straight trajectory rather than those which are completely deviated with the wall jet or in the slot.

Similar fluctuating-pressure frequencies were

obtained in the spaces above and underneath the impingement wall.

As a conclusion, attempts to control and/or eliminate turbulent noise generation, in configurations similar to that considered in the present study, should focus on the behavior of the opposite vortices that tend to move in phase without considerable deviation from the central plane of the free-shear layers surrounding the plane jet.

This study represents a platform for a simulation of the corresponding acoustic field using more elaborate computational resources and numerical tools.

ACKNOWLEDGEMENTS

The authors are grateful to the Petroleum Institute of Abu Dhabi for providing High Performance Computing facilities.

REFERENCES

- ANSYS Inc. (2015). *Fluent User Guide and Fluent Theory Guide*, version 16.2.
- Assoum, H. (2013). *Etude expérimentale des couplages entre la dynamique d'un jet qui heurte une plaque fendue et l'émission sonore générée*, PhD Thesis, La Rochelle University, La Rochelle, France (In French).
- Billon, A., V. Valeau and A. Sakout (2005). Two feedback paths for a jet-slot oscillator, *J. Fluids Struct.* 21, 121-132.
- Bodony, D. J. and S. K. Lele (2008). Current status

- of jet noise predictions using Large-Eddy Simulation *A.I.A.A. J.*, 46, 364-380.
- Celik, I. B., Z. N. Cehreli and I. Yavuz (2005). Index of resolution quality for large eddy simulations, *J. Fluids Eng.* 127, 949-958.
- Ghosal, S. (1999). Mathematical and physical constraints on large-eddy simulation of turbulence, *A.I.A.A. J.* 37, 425-433.
- Hadžiabdić, M. and K. Hanjalić (2008). Vortical structures and heat transfer in a round impinging jet, *J. Fluid Mech.* 596, 221-60.
- Ho, C. M. and N. S. Nosseir (1981). Dynamics of an impinging jet. Part 1. The feedback phenomenon, *J. Fluid Mech.* 105, 119-142.
- Matsuura, K. and M. Nakano (2011). Direct computation of a hole-tone feedback system at very low Mach numbers, *J. Fluid Sci. Technol.* 6, 548-561.
- Matsuura, K. and M. Nakano (2012). A throttling mechanism sustaining a hole tone feedback system at very low Mach numbers, *J. Fluid Mech.* 710, 569-605.
- Matsuura, K. and M. Nakano (2014). Disorganization of a hole tone feedback loop by an axisymmetric obstacle on a downstream end plate, *J. Fluid Mech.* 757, 908-942.
- Pope, S. (2000). *Turbulent flows*, Cambridge University Press, Cambridge.
- Sagaut, P. (2006). *Large-eddy simulation for incompressible flows - An introduction*, Scientific Computation series, Springer-Verlag, Berlin.
- Shuja, S. Z., B. S. Yilbas and M. O. Budair (2007). Jet impingement on cylindrical cavity: Conical nozzle considerations, *J. Fluids Struct.* 23, 1106-1118.
- Tam, C. K. W. (2004). Computational aeroacoustics: An overview of computational challenges and applications, *Int. J. Comput. Fluid Dyn.* 18, 547-567.
- Tam, C. K. W., H. Ju and B. E. Walker (2008). "Numerical simulation of a slit resonator in a grazing flow under acoustic excitation", *J. Sound Vibr.* 313, 449-471.
- Tam, C. K. W., H. Ju, M. G. Jones, W. R. Watson and T. L. Parrott (2005). A computational and experimental study of slit resonators, *J. Sound Vibr.* 284, 947-984.
- Versteeg, H. and W. Malalasekera (2007). *An introduction to computational fluid dynamics: the finite volume method*, Pearson Education Limited. Edinburgh Gate. Harlow. Essex CM20 2JE.
- Yokoyama, H., M. Kobayashi, H. Onitsuka, A. Miki and A. Iida (2014). Direct numerical simulation of flow and acoustic fields around an air-reed instrument with tone holes, proceedings of 43rd International Congress on Noise Control Engineering, (inter.noise 2014), Melbourne, Australia, November.
- Ziada, S. (2002). Active stabilization of a planar jet impinging on a flexible wedge, *J. Fluids Struct.* 16(5), 613-626.